Semiconducting Heusler Compounds beyond the Slater-Pauling Rule

Michael Parzer,[1,*] Fabian Garmroudi,[1] Alexander Riss,[1] Michele Reticcioli,[2] Raimund Podloucky,[3] Michael Stöger-Pollach,[4] Evan Constable,[1] Andrej Pustogow,[1] Takao Mori,[5,6] and Ernst Bauer[1]

[1] *Institute of Solid State Physics, Technische Universität (TU) Wien, Vienna 1040, Austria*

[2] *Faculty of Physics and Center for Computational Materials Science, University of Vienna, Vienna 1090, Austria*

[3] *Department of Physical Chemistry, University of Vienna, Vienna 1090, Austria*

[4] *University Service Center for Transmission Electron Microscopy, TU Wien, Vienna 1040, Austria*

[5] *International Center for Materials Nanoarchitectonics (WPI-MANA), National Institute for Materials Science, Tsukuba, Ibaraki 305-0044, Japan*

[6] *Graduate School of Pure and Applied Sciences, University of Tsukuba, Tsukuba, Ibaraki 305-8571, Japan*

(Received 4 January 2024; revised 20 August 2024; accepted 23 August 2024; published 20 September 2024)

Heusler compounds with semiconducting properties represent an important class of functional materials. Usually, research on these systems is guided by simple electron-counting rules, such as the Slater-Pauling principle. Here, we report on the discovery of Heusler-type semiconductors, significantly deviating from the Slater-Pauling rule. We theoretically predict the occurrence of nonmagnetic semiconducting ground states in various highly off-stoichiometric full-Heusler alloys, where self-substitution leads to a band-gap opening. This unexpected trend is confirmed experimentally by thermoelectric transport measurements on a multitude of $Fe_{2-2x}V_{1-x}Al_{1+3x}$ samples with up to 20% substitution of Fe and V atoms. The band-gap opening leads to an exceptionally large Seebeck coefficient in p-type Fe_2VAl thermoelectrics, previously limited by bipolar conduction and low-density-of-states effective mass. Consequently, our work presents a paradigm to tune the band gap of Heusler compounds by self-substitution and introduces a hitherto unexplored class of semiconductors with exceptional thermoelectric properties, offering significant potential for advancements in energy science and sustainable-energy technologies.

DOI: 10.1103/PRXEnergy.3.033006

I. INTRODUCTION

Heusler compounds in the X_2YZ (full-Heusler) and XYZ (half-Heusler) stoichiometry constitute one of the richest material classes [1], encompassing over 1000 different intermetallics with diverse physical and electronic properties, such as half-metallicity [2], nontrivial band topology [3], superconductivity [4], or semiconducting states. Recently, discoveries of a giant anomalous Nernst effect due to a large variety of new topological phases have sparked further interest in these compounds [5]. Thus, potential applications of Heusler compounds reach from the field of spintronics [6] and magnetism [7] toward photovoltaics [6] and thermoelectrics [8,9]. For energy technologies such as photovoltaics and thermoelectrics, the highly tunable band gaps of half-Heusler compounds are particularly advantageous, positioning them as some of the most promising materials for thermoelectric applications. In contrast, full-Heusler compounds typically have smaller band gaps, limiting their direct application in energy technologies. Nevertheless, full-Heusler compounds, especially Fe_2VAl-based materials, continue to attract significant research interest due to their cost-effective constituents and favorable mechanical properties [10–17]. The development of strategies to modify the electronic structure of full-Heuslers is crucial for unlocking their full potential.

Notably, the electronic structure of Heusler compounds depends mainly on the valence electron concentration per atom (VEC), which in turn can be used to effectively and reliably predict and tune the electronic as well as the magnetic ground state [1]. For instance, Heusler compounds with exactly six valence electrons per atom are typically semiconductors with vanishing magnetic moment m, whereas m increases linearly for VEC $\lesssim 6$ (see Fig. 1). This is subsumed in the well-known Slater-Pauling (S-P) rule, which was originally developed by Slater and Pauling

*Contact author: Michael.parzer@tuwien.ac.at

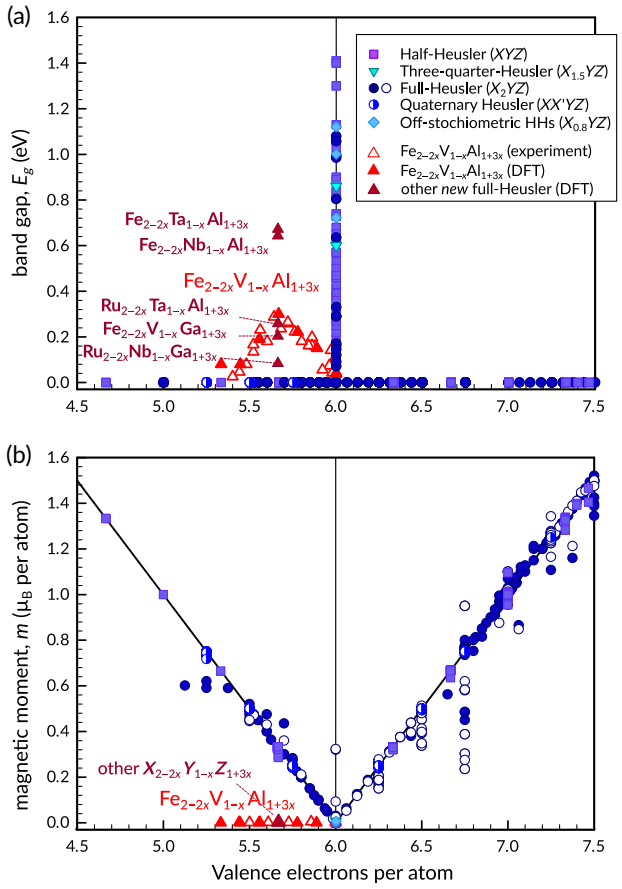

FIG. 1. Deviation from the Slater-Pauling (S-P) rule. (a) The reported band gap E_g and (b) magnetic moment m of various types of Heusler alloys as a function of the number of valence electrons per atom. The filled symbols depict theoretical values, while the open symbols are values found experimentally. All compounds fall on a single line for the *regular* Heusler compounds in panels (a) and (b), which is commonly described by the S-P rule. The strongly off-stoichiometric Heusler compounds presented here are an exception and do not follow this universal rule for a higher concentration of the Z element. This has also been confirmed experimentally for $Fe_{2-2x}V_{1-x}Al_{1+3x}$, as shown by the open red symbols. The magnetic measurements depicted in (b) are presented in detail in Appendix C 1, while the referenced table with the depicted values for E_g and m extracted from literature is attached as Supplemental Table [18].

to comprehend the electronic and magnetic properties of simple transition-metal alloys [19,20] and has later been summarized for full-Heusler compounds by Galanakis *et al.* [2]. Exceptions to this rule are rare, with only special cases such as the eight-electron half-Heuslers (HHs) [21] or the *R*NiSb compounds with a VEC of ≥ 9 [22], deviating from the conventional S-P behavior. Heusler compounds with a VEC close to 6 generally fulfill the S-P rule, regarding their electronic and magnetic structure. This fact is illustrated in Fig. 1, which shows the calculated energy band gaps and magnetic moments of hundreds of Heusler-type compounds as a function of their VEC. It can be seen that VEC = 6 marks an insulating nonmagnetic singularity in a vast sea of adjacent magnetic metals. A comprehensive list of all members of the Heusler family in Fig. 1 that satisfy the S-P rule is in the Supplemental Table [23]. The relevant papers [24–87] have been collected employing conventional search engines as well as natural-language-processing tools as implemented in DIMENSIONS.AI [88].

In HHs with VEC = 6, yielding 18 electrons per formula unit (f.u.), the most electropositive element donates its valence electrons, resulting in closed shells on all atoms, a finite band gap, and a zero magnetic moment, in agreement with the S-P rule. It follows naturally that changing the number of electrons by chemical substitution would destabilize the compounds and would result in a shift of the Fermi level out of the gap. Hence, the majority of stable HH compounds feature a valence electron count of six per atom [89]. For full-Heusler materials, the outer d shells of the X and Y elements are not fully filled. The band gap results from the splitting of their d states into e_g and t_{2g} orbitals due to the crystal field of their surroundings. This leads to much smaller band gaps in this class of materials. In fact, for full-Heusler materials, band gaps have only been reported in unstable or metastable compounds such as Fe_2NbAl [90] or Fe_2TiSi [91]. The nature of the chemical bonding in Heusler compounds rationalizes the validity of the S-P rule as a simple chemical electron-counting rule.

Moreover, guided by the S-P rule, novel Heusler-type semiconductors have been discovered in recent years. Some noteworthy examples with promising thermoelectric properties include so-called double half-Heuslers ($X_2YY'Z_2$), such as $Ti_2FeNiSb_2$ [92], three-quarter Heuslers ($X_{1.5}YZ$), e.g., $Ru_{1.5}ZrSb$, with 21 valence electrons [93], or off-stoichiometric variations such as $Nb_{0.84}CoSb$. Interestingly, these vacancy-afflicted half-Heusler compounds were first described as stoichiometric 19-valence electron compounds [94,95].

After thorough investigation, however, it was found that NbCoSb crystallizes with vacancies as $Nb_{0.8}CoSb$ (VEC = 6) and has excess elemental Nb impurities [32,96,97]. Therefore, crucially, all of these examples satisfy the S-P rule, as can be seen in Fig. 1.

Here, we report on the discovery of strongly off-stoichiometric full-Heusler compounds, which form a band gap and therefore show significant deviations from the S-P rule with respect to both their electronic and their magnetic properties [see the red symbols in Figs. 1(a) and 1(b)]. The commonly used presentation of the magnetic moment per atom versus the VEC fails to follow the S-P relation for the $X_{2-2x}Y_{1-x}Z_{1+3x}$ alloys, as none of the compounds are magnetic. Moreover, when increasing x up to $x = 0.11$ (VEC = 5.65), a significant band-gap opening is observed, also contradicting the S-P rule with

regard to their electronic structure. Full-Heusler *semiconductors*, although predicted theoretically, have not been experimentally realized so far as bulk materials as they are either semimetallic, such as Fe_2VAl and Fe_2VGa [98], or metastable, such as Fe_2NbAl [90] or Fe_2TiSi [91]. Therefore, our findings present a propitious approach toward achieving highly off-stoichiometric, yet stable, full-Heusler semiconductors. By combining efforts of density-functional-theory (DFT) calculations and thermoelectric transport as well as magnetic experiments on a large number of samples, we demonstrate that off-stoichiometric full-Heusler compounds with a $X_{2-2x}Y_{1-x}Z_{1+3x}$ stoichiometry exhibit semiconducting properties if the additional Z atoms are incorporated as antisite defects on the X and Y sites [see Fig. 2(a)]. In the following, the theoretical and experimental evidence for this unexpected violation of the S-P rule will be presented.

II. MATERIALS AND METHODS

A. Computational details

DFT calculations were conducted using the Perdew-Burke-Enzerhof (PBE) general-gradient approximation as implemented in the Vienna *ab initio* simulation package (VASP) [99–104]. To simulate the disorder, $3 \times 3 \times 3$ supercells with a total of 108 atoms were created for the substituted cases. For different substitutions, the appropriate number of X and Y atoms from the respective lattice site were replaced with the Z atoms. The supercells were then relaxed regarding their volume as well as atomic positions, employing a $5 \times 5 \times 5$ k-mesh and an energy-cutoff value of 450 eV. For the self-consistent calculations, a finer k mesh of $8 \times 8 \times 8$ was used, to reduce the noise in the electronic density of states (DOS). We used the tetrahedron method with Blöchl corrections to set the partial occupancies for each orbital.

To extract the partial DOS of Al atoms sitting at different lattice sites, i.e., Al_{Fe}, Al_V, and Al_{Al}, a disambiguation of these atoms was implemented into the POSCAR structure file. The Bader volumes extracted from the regular self-consistent calculation were approximated to be spherical and the Wigner-Seitz radius of the respective atoms were adjusted accordingly. The element-decomposed DOS is depicted in Fig. 3(b), normalized with the number of atoms per element in the unit cell.

B. Synthesis and characterization

All samples analyzed in this work were synthesized under an argon atmosphere using a high-frequency induction-melting furnace. The samples were weighed using a high-precision scale and elements with a purity of 99.99%, 99.95%, and 99.999% for Fe,V and Al, respectively. The mass loss was below 0.1% for all samples, yielding well-defined stoichiometry in our samples, which was also checked by X-ray fluorescence for selected samples in an earlier work [105]. The XRD patterns were measured using a commercial device from PANalytical and the lattice parameters were extracted via Rietveld refinements as implemented in PowderCell (see Appendix B 1). Electron microscopy was performed using an FEI Quanta 250 field-emission gun (FEG) scanning electron microscope (SEM) and an FEI TECNAI F20 FEG transmission electron microscope, as available at the USTEM research facility [106].

C. Thermoelectric measurements

Transport measurements above room temperature were conducted on bar-shaped samples using the ZEM-3 from ULVAC RIKO. Low-temperature Seebeck coefficients were measured on the same samples using a home-made setup inside a He-bath cryostat, employing the seesaw-heating technique [107] to cancel out interfering voltages, similar to other works [108,109]. Low-temperature resistivity measurements were conducted using the four-point measurement within a He-bath cryostat. The low-temperature Seebeck and resistivity data were adjusted to the high-temperature measurement by multiplying by a constant factor in the range of $0.95 < x < 1.05$ to account for the slight mismatch in absolute values.

D. Analysis of transport data

The temperature-dependent Seebeck-coefficient data were analyzed using a three-parabolic band model within the framework of the Landauer theory. Assuming acoustic phonon and alloy-disorder scattering, the dependence of the energy on the carrier scattering time is given by

$$\tau(E,T) \propto \tau_0(T) E^{-1/2}, \tag{1}$$

where τ_0 depends on the type of scattering process [110]. As for the Seebeck coefficient, any energy-independent prefactors cancel out; hence $S(T)$ of a single band can be described by Fermi integrals of the first and zeroth order, as [10,110]

$$S(T) = \frac{k_B}{e}\left[\eta - \frac{F_1(\eta,T)}{F_0(\eta,T)}\right], \tag{2}$$

where η is the chemical potential, T is the temperature, e is the elementary charge, and F_n is the respective Fermi integral:

$$F_n(\eta,T) = \int_0^\infty \frac{\xi^n d\xi}{1 + e^{(\xi-\eta)}}. \tag{3}$$

Considering multiple bands, the total Seebeck coefficient S_t can be calculated by adding up the single-band

contributions weighted with their conductivity, using

$$S_t = \frac{\Sigma_n S_n \sigma_n}{\Sigma_n \sigma_n}, \tag{4}$$

where $\sigma_n \propto 1/m_n$ is inversely proportional to the respective band mass m_n. Assuming that, in total, three bands are relevant for transport, this leads to five fitting parameters, including the position of the Fermi level E_F with respect to the first band, the position of the other two bands with respect to the first band, E_{g2} and E_{g3}, and the relative weighting parameters, σ_2 and σ_3, of the respective bands. The position of the first band is set to 0 and the relative weighting parameter σ_1 to -1, as the other values are relative to these and E_{g1} and σ_1 can be chosen arbitrarily without affecting the results. The closest distance of the bands at the band gap, either E_{g1} or E_{g2}, denotes the effective band gap of the compound extracted from the model, which is plotted in Fig. 5(c). The resulting fitting parameters of all analyzed samples are given in Table S2 of the Supplemental Material [23].

III. ELECTRONIC STRUCTURE

To determine the electronic DOS of $X_{1.78}Y_{0.89}Z_{1.33}$, depicted in Fig. 3, reasonably large supercells containing 108 atoms, with six Z_X and three Z_Y antisites, were constructed. For $Fe_{2-2x}V_{1-x}Al_{1+3x}$, this was shown to be the most favorable arrangement [111,112]. For comparison with experimental data, we put special emphasis on the calculation of this system. Calculations on small numbers of different antisites conducted in the past have found detrimental effects of the substitutions on the electronic band gap of full-Heusler compounds. [111–114] Nonetheless, for all considered full-Heusler compounds, we have found a band-gap opening if the Z atoms are distributed evenly on the X and Y sites as antisites, even for large substitutions (see Fig. 1).

For $Fe_{1.78}V_{0.89}Al_{1.33}$, a total of 15 randomized antisite configurations were calculated in this way and averaged, weighted with their formation energy, employing the Boltzmann average:

$$\mathrm{DOS_{av}} = \frac{\Sigma_{n=1}^{15} \mathrm{DOS}_n e^{(-E_{\mathrm{form},n})/k_B T)}}{\Sigma_{n=1}^{15} e^{(-E_{\mathrm{form},n})/k_B T)}}, \tag{5}$$

where $E_{\mathrm{form},n}$ is the respective formation energy, DOS_n is the respective electronic DOS, T is the averaging temperature, and k_B is the Boltzmann constant. The results for different averaging temperatures T are depicted in Fig. 2, together with the formation energy as a function of the electronic energy gap. The randomization of the antisite positions was done using *true* random numbers employing atmospheric noise [115]. The resulting DOSs were then averaged using these Boltzmann weights to obtain a robust result (for details, see the Supplemental Material [23]), which is depicted in Fig. 3(a) and reveals striking changes in the electronic structure with Al self-substitution. Notably, at the highest averaging temperature (11 000 K), the formation energies are largely disregarded, resulting in a more uniform averaging of the DOSs.

For the other stoichiometries varying in Al concentrations, we started from the most favorable supercell of $Fe_{1.78}V_{0.89}Al_{1.33}$ and added or removed antisite defects to create supercells for different x values. Again, different

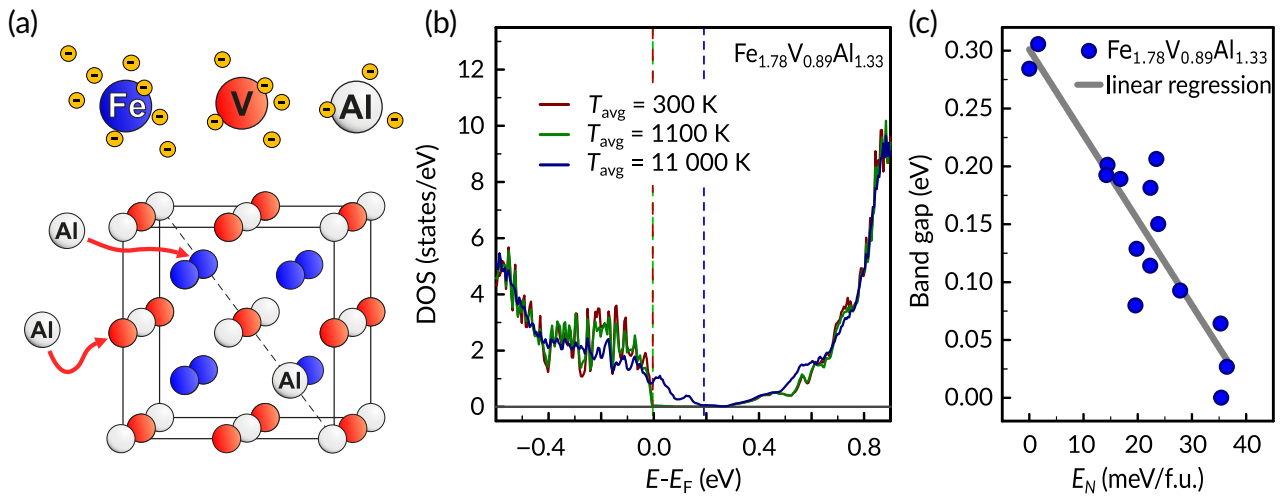

FIG. 2. The analysis of the different antisite configurations of $Fe_{1.78}V_{0.89}Al_{1.33}$. (a) A sketch of the full-Heusler crystal structure of Fe_2VAl, with Al replacing Fe and V atoms on random lattice sites. (b) The Boltzmann-averaged DOS over all 15 supercells for different averaging temperatures. The energetically less favorable antisite configurations are only relevant for the highest averaging temperature of 11 000 K. (c) The correlation of the extracted band gap with the configuration energy of the different supercells, normalized to the most favorable one: $E_N = E_{\mathrm{form},n} - E_{\mathrm{fav}}$. Evidently, the more favorable antisite configurations exhibit larger band gaps. The linear regression acts as a guide to the eye.

antisite configurations were tested to assess the influence of the antisite positions on the electronic structure for different x. The unfolded band structures for different stoichiometries ranging from $x = 0$ to $x = 0.22$ are displayed in Appendix A. For stoichiometric Fe_2VAl, our calculations reveal a profound pseudogap, aligning with recent literature observations [9,14,116]. Notably, the introduction of Al into the compound induces substantial changes in the DOS at the valence-band edge, accompanied by a band-gap opening of approximately 0.3 eV. As illustrated in the inset, the number of electrons per atom is reduced from 6 to 5.65, in agreement with the diminished number of electrons in the valence band. One can clearly see that the Fermi level E_F, however, remains in the energy gap for the highly off-stoichiometric $Fe_{1.78}V_{0.89}Al_{1.33}$. Moreover, when testing the effect of different values of the on-site Coulomb interactions $U - J$, we have found only negligible changes in the electronic structure for the off-stoichiometric compounds.

The partial DOS of $Fe_{1.78}V_{0.89}Al_{1.33}$ depicted in Fig. 3(b) reveals that, remarkably, aluminum atoms still contribute very few states to the DOS close to the Fermi energy, even for the compound with $x = 0.11$, for which Al atoms make up one third of all atoms in the supercell. Instead, the sharp rise in the DOS below E_F is constituted by resonant localized states, attributable to all constituent elements of the compound. Hence, the changes in the electronic structure can be understood as changes to the hybridization between the constituent elements by the Al substitution, rather than as addition of Al impurity states to the DOS. Out of the Al atoms, evidently, the Al_{Fe} antisites feature the largest contribution to the DOS per atom around E_F. To further elucidate the changes in the electronic structure caused by the Z-element off-stoichiometry, we have calculated the unfolded band structure of the most stable supercells for several members of the Heusler family using BANDS4VASP [117,118]. The band structures of $Fe_{1.78}V_{0.89}Al_{1.33}$ and

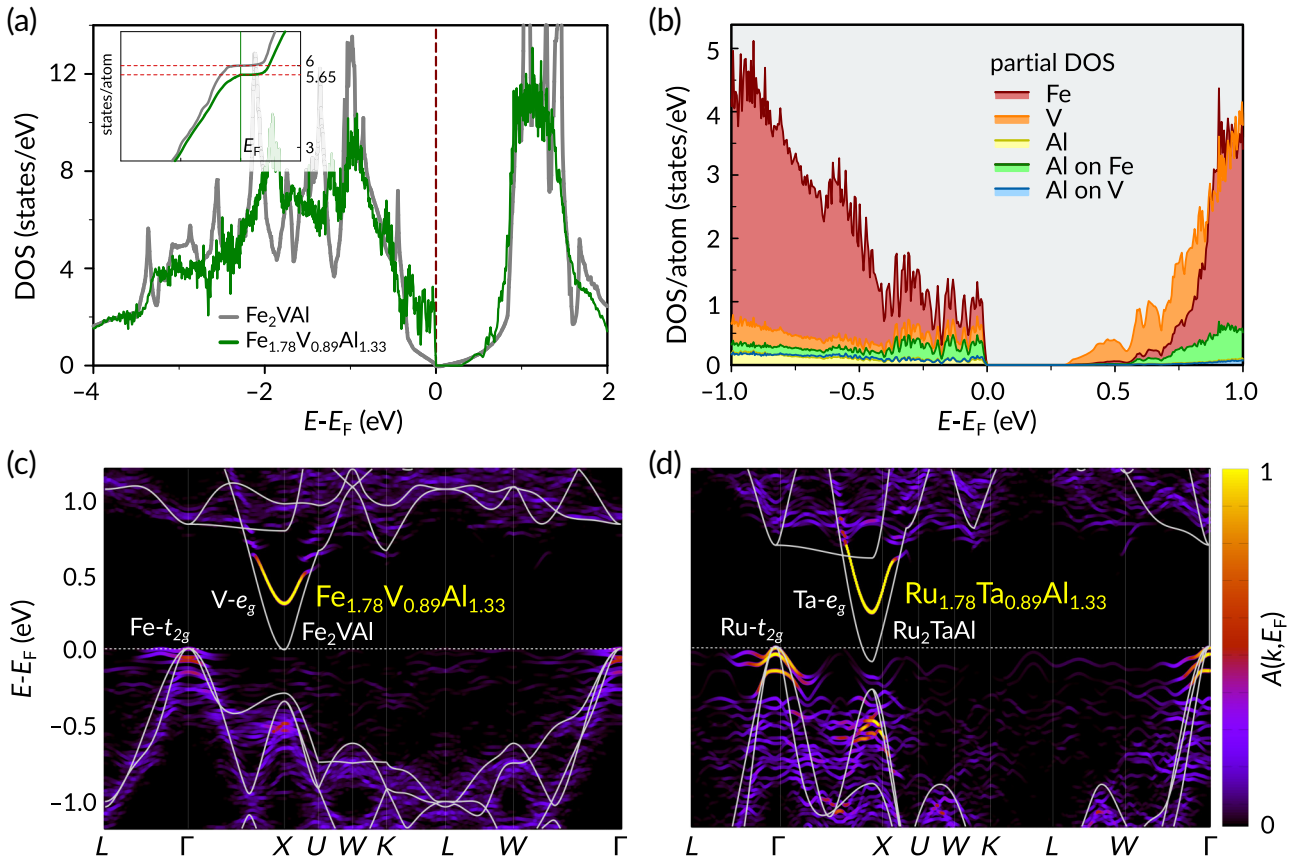

FIG. 3. The electronic structure of strongly off-stochiometric full-Heusler compounds $X_{2-2x}Y_{1-x}Z_{1+3x}$. (a) A schematic of the full-Heusler crystal structure, with additional Z atoms occupying the X and Y lattice sites as antisite defects. (b) A comparison of the electronic density of states (DOS) of pristine Fe_2VAl and averaged $Fe_{1.78}V_{0.89}Al_{1.33}$. A strong change in the DOS at the Fermi level E_F is observable, together with the opening of an energy gap. The inset reports the integrated DOS in states per atom, showing a decrease of the total number of states per atom in $Fe_{1.78}V_{0.89}Al_{1.33}$ below E_F. (c),(d) The unfolded band structure of two novel semiconductors, (c) $Fe_{1.78}V_{0.89}Al_{1.33}$ and (d) $Ru_{1.78}Ta_{0.89}Al_{1.33}$. The color code depicts the spectral function $A(k, E_F)$ obtained from the unfolding calculations. For better comparison, the band structure of the parent stoichiometric compounds is superimposed as a white solid line.

$Ru_{1.78}Ta_{0.89}Al_{1.33}$ are shown in Figs. 3(c) and 3(d), as two representative examples. Compared to their stoichiometric full-Heusler counterpart, a significant broadening of the dispersive conduction band is observable, effectively shifting the edge toward higher energies. For both compounds, this leads to the opening of an indirect band gap of the order of 0.3 eV, while E_F remains pinned at the valence-band edge within the band gap. Notably, this semiconducting ground state constitutes a significant deviation from the S-P behavior for full-Heusler materials.

Hybridization-induced band gaps in transition-metal aluminides have been discussed by Weinert and Watson [119]. Besides $RuAl_2$ and $FeAl_2$, they have also investigated Fe_2VAl, tracing back the (pseudo) band gap to hybridization between the transition metals (TMs) and Al on the one hand and the lack of Al-TM *d*-*d* hybridization on the other. In our off-stoichiometric Heusler compound, this effect is increased by the additional Al substitution on Fe-V sites. As the Al_V antisites have their *d* states at much higher energies than V, the V—V bonds are disturbed, leading to the observed broadening of the conduction band at the X point [as evident from Fig. 3(c)]. Focusing on the Fe states that dominate the valence band, the Al antisites lead to a sizable loss of coordination between Fe atoms, penalizing the orbital hybridization. As a consequence, the Fe states become more localized, giving rise to flat Fe bands, akin to resonant levels, at the Γ point. Similar considerations can be drawn for $Ru_{1.78}Ta_{0.89}Al_{1.33}$ in Fig. 3(d) and for other full-Heuslers, such as $Fe_{1.78}V_{0.89}Ga_{1.33}$ and $Fe_{1.78}Nb_{0.89}Al_{1.33}$, where the chemical bonding works in a similar manner. We note that such flat bands at the Fermi energy are of great interest in fundamental solid-state physics, as the small kinetic energy of charge carriers compared to the Coulomb interaction can give rise to exotic quantum phases of matter [120,121]. Indeed, we have observed peculiar anomalies in various low-temperature transport properties that will remain a subject for future studies.

IV. EXPERIMENTAL RESULTS

To confirm the DFT calculations, we synthesized a multitude of $Fe_{2-2x}V_{1-x}Al_{1+3x}$ samples with the amount of Al substitution reaching from $x = 0$ to $x = 0.2$ (Fe_2VAl–$Fe_{1.6}V_{0.8}Al_{1.6}$). In Fig. 4(a), we display the structural properties of stoichiometric Fe_2VAl in comparison to off-stoichiometric $Fe_{1.78}V_{0.89}Al_{1.33}$. As evidenced by X-ray powder diffraction, both compounds crystallize in the $L2_1$ full-Heusler structure, as all peaks are clearly present. The evolution of the experimentally determined lattice parameter with increasing x shows linear behavior, indicating full solubility along the transition. The slight disparity in absolute values of the lattice parameter between DFT and experiment is a known anomaly in Fe_2VAl, which has been reported in the literature

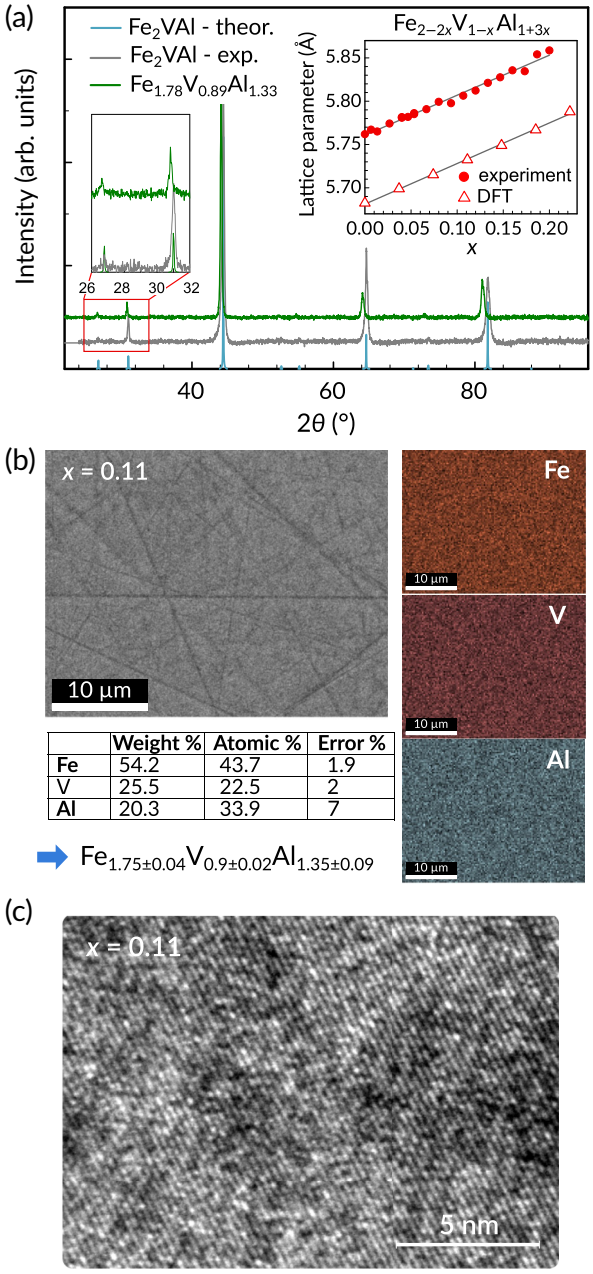

FIG. 4. The structural analysis of $Fe_{2-2x}V_{1-x}Al_{1+3x}$. (a) The X-ray diffraction (XRD) patterns of Fe_2VAl and $Fe_{1.78}V_{0.89}Al_{1.33}$; all peaks of the $L2_1$ structure are clearly visible, without any impurity peaks. The inset on the right shows the comparison of the experimental lattice parameters of $Fe_{2-2x}V_{1-x}Al_{1+3x}$, extracted from Rietveld refinements, with the lattice parameters obtained from the DFT calculations. (b) Thr electron-dispersive X-ray spectroscopy (EDX) of the sample $Fe_{1.78}V_{0.89}Al_{1.33}$. The scanning electron microscopy (SEM) image and the EDX mapping of the three elements Fe, V, and Al on the right exclude any impurity phases. The total composition was determined to be $Fe_{1.75}V_{0.9}Al_{1.35}$. Panel (c) depicts a TEM image at very large magnifications for the same sample, confirming that the main matrix of the compound is single phase and homogeneous at the nanoscale.

previously [98,111,122,123]. Moreover, the slope of the concentration-dependent increase of the lattice parameter agrees remarkably well with that extracted from DFT calculations, as depicted in the inset. The high tolerance toward a large degree of antisite disorder in Fe_2VAl is well known and likely results from the similar sizes of the atomic radii and the highly symmetrical cubic crystal structure. For the $Fe_{2-2x}V_{1-x}Al_{1+3x}$ compounds, the stability is possibly increased further by the band-gap opening, as it separates bonding from antibonding states. The composition and homogeneity of these samples were confirmed by energy-dispersive X-ray spectroscopy (EDX) and transmission electron microscopy (TEM), as shown in Figs. 4(b) and 4(c). The EDX measurements reveal that samples such as $Fe_{1.78}V_{0.89}Al_{1.33}$ maintain the intended stoichiometry without detectable microscale impurities. The TEM measurements further confirm the absence of nanoscale impurities, aside from minor V_4Al_4C precipitates accounting for less than 1% of the volume (see Appendix B). This high degree of compositional homogeneity, even at the nanoscale, is crucial for accurately assessing the thermoelectric properties and understanding the electronic structure for materials optimization.

Narrow-gap semiconductors, such as those predicted theoretically in Fig. 3, are of great interest for energy applications such as thermoelectrics, which seamlessly convert heat into electricity and vice versa. It is well known that $S(T)$ of narrow-gap semiconductors strongly depends on the band gap [128]. Therefore, we have studied the temperature- and composition-dependent thermoelectric properties of a large number of $Fe_{2-2x}V_{1-x}Al_{1+3x}$ samples. In Fig. 5, we show the experimental data for the Seebeck coefficient as a function of the temperature and the VEC. Moreover, we compare the band gap extracted from the experimental $S(T)$ curves by employing a triple parabolic band model with the prediction from DFT calculations, assuming alloy disorder and acoustic phonon scattering. Inspecting the $S(T)$ of $Fe_{2-2x}V_{1-x}Al_{1+3x}$ in Fig. 5(a), it can be seen that the maximum Seebeck coefficient S_{max} is increased significantly (by approximately 100%) for the Al off-stoichiometry of $x = 0.11$.

Simultaneously, the temperature of the maximum T_{max} is shifted toward higher values, from about 200 K for Fe_2VAl to about 400 K for $Fe_{1.78}V_{0.89}Al_{1.33}$. These systematic changes in $S(T)$ are typical for an increase of the band gap. Indeed, by using the triple parabolic band model to fit the experimental $S(T)$ curves, a tiny band gap, $E_g \sim 0.02$ eV, is found for pristine Fe_2VAl, but a sizable E_g of about 0.3 eV is found for strongly off-stoichiometric $Fe_{1.78}V_{0.89}Al_{1.33}$. These values are very consistent with those predicted theoretically by our *ab initio* band-structure calculations [see Figs. 3(c) and 3(d) as well as by Refs. [9,123]]. The main difference between the DFT and the experimentally derived electronic structures

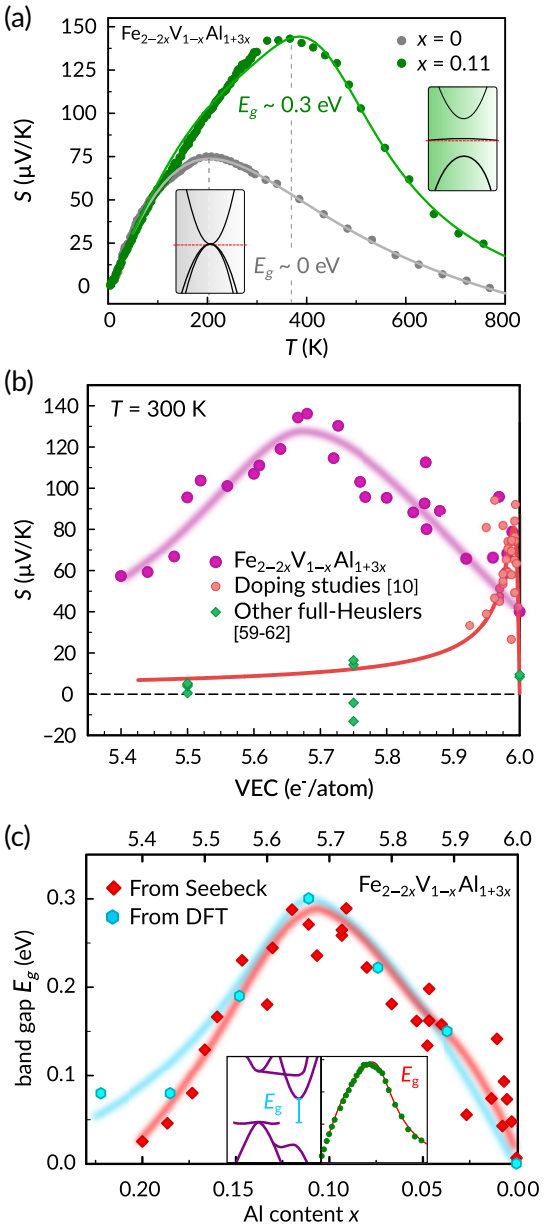

FIG. 5. The experimental results for $Fe_{2-2x}V_{1-x}Al_{1+3x}$. (a) The experimental data of the temperature-dependent Seebeck coefficient for $x = 0$ and $x = 0.11$ in gray and green, respectively. The solid lines depict the three parabolic band model fit, applied to assess the effective band structure close to E_F as sketched in the insets. The data and the fitting results for all samples are shown in Appendix C 2. (b) The Pisarenko-style plot at $T = 300$ K reveals a significant deviation from the S-P behavior demonstrated in doping studies [10], and for other full-Heuslers [124–127], when plotting raw Seebeck data versus the valence electron count per atom (VEC). (c) The composition-dependent behavior of the band gap extracted from fitting experimental $S(T)$ curves and DFT calculations (see Appendix A), respectively. The trend follows the raw Seebeck values at $T = 300$ K depicted in (b). For both, the band gap E_g increases with increasing Al concentration up to a maximum at around $x = 0.11$ and VEC = 5.65, before decreasing again for higher Al concentrations.

is the different position of the Fermi level, with E_F slightly doped into the valence band for the latter. This can most likely be explained by a low concentration of V_{Fe} antisite defects present in the samples, as rationalized by additional calculations depicted in Fig. S2D of the Supplemental Material [23].

In Fig. 5(b), we show the room-temperature Seebeck coefficient of $Fe_{2-2x}V_{1-x}Al_{1+3x}$ as a function of the valence electron concentration per atom, compared to previous doping studies in Fe_2VAl-based compounds as well as other members of the full-Heusler family. It can be seen that in contrast to the predicted vanishing Seebeck effect for conventional doping, an anomalous increase of the Seebeck coefficient is obtained at VEC ≈ 5.65, which corresponds to the off-stoichiometric composition $Fe_{1.78}V_{0.89}Al_{1.33}$. Indeed, not only does the enhanced Seebeck coefficient constitute a record among p-type full-Heusler compounds but it also signifies a severe deviation from the rigid-band-doping scenario as well as the S-P rule (red solid line). Notably, for p-type Fe_2VAl-based compounds, increasing the band gap and therefore the Seebeck coefficient is one of the key targets to improve thermoelectric performance and bring these compounds closer to application [9,129]. Previous p-type doping studies in Fe_2VAl thermoelectrics have achieved Seebeck coefficients up to 110 μV/K, which represents a significant bottleneck for achieving competitive TE performance with their n-type counterparts: a simple estimation of the maximum figure of merit zT of Fe_2VAl-based compounds with a Seebeck coefficient of 110 μV/K versus compounds with $S_{max} = 150$ μV/K reveals a doubling of zT_{max} from 0.64 to 1.27 [130] when neglecting the lattice thermal conductivity.

This has motivated us to theoretically study the unfolded band structures of off-stoichiometric $Fe_{2-2x}V_{1-x}Al_{1+3x}$ at different Al concentrations to investigate the evolution of the band gap and the electronic structure near E_F, with varying stoichiometry. In Fig. 5(c), we show a comparison of the band gaps from DFT calculations (Appendix A) with those obtained by modeling numerous experimental $S(T)$ curves of $Fe_{2-2x}V_{1-x}Al_{1+3x}$, using a triple parabolic band model (for the complete set of temperature-dependent Seebeck-coefficient data, see Appendix C) [9,10,116]. We find a remarkable agreement not only in terms of absolute values but especially regarding the overall domelike shape and pronounced peak at $x \sim 0.11$. For higher Al substitutions, the flat impurity bands are shifted into the band gap, effectively reducing E_g. Moreover, for $0.05 < x < 0.17$, the fitting model yields an additional flat valence band close to E_F, which is reminiscent of the unfolded band structures of those compounds, depicted, e.g., in Fig. 3(c) and also in Appendix A. The band gaps extracted independently from the temperature-dependent resistivity applying the Arrhenius law also confirm this behavior, as shown in Appendix C 3.

V. CONCLUSIONS

In summary, we have found an unexpected band-gap opening in off-stoichiometric Heusler compounds $X_{2-2x}Y_{1-x}Z_{1+3x}$ with $x > 0$, in contradiction to the S-P rule. The similarity of the electronic structure determined by independent experimental methods for $Fe_{2-2x}V_{1-x}Al_{1+3x}$ corroborates our theoretical predictions and constitutes solid evidence for the emergence of a semiconducting nonmagnetic ground state in these systems. This not only opens a new avenue for tuning the electronic structure of full-Heusler compounds but also brings Fe_2VAl-based compounds closer to practical thermoelectric applications due to the substantial increase in $S(T)$. Compared with the existing literature on p-type full-Heusler compounds, the Seebeck values reported here constitute record-high values, exceeding those of existing materials by over 20%, without targeted material optimization. Therefore, we conclude that the ultrahigh off-stoichiometry with respect to the Z element constitutes a general approach to achieve stable full-Heusler semiconductors with promising thermoelectric properties. This approach significantly extends the phase space of ternary Heusler compounds as functional materials and could lead to the discovery of multiple so-far-unexplored systems with intriguing physical properties, helping to satisfy the need for optimized electronic materials in the field of energy sciences. Not only is it remarkable that semiconducting states are found beyond the S-P principle but it is also unique that such types of electronic band structures can be found in heavily disordered structures.

ACKNOWLEDGMENTS

The computational results presented have been achieved using the Vienna Scientific Cluster (VSC). We acknowledge the TU Wien X-Ray Center (XRC) for the measurement time for the structural analysis of our samples. We acknowledge the University Service Facility for Transmission Electron Microscopy (USTEM) facility at TU Wien for the electron-microscopy measurements. Funding came from the Japan Science and Technology Agency (JST) program MIRAI, via Grant No. JPMJMI19A1.

M.P. and F.G. conceptualized the work and planned the outline of the draft. M.R., R.P., and M.P. conceptualized the theoretical study and interpreted and discussed the DFT results. M.P. did the DFT calculations. M.P. synthesized the samples and did the experiments. M.P., F.G., A.R., A.P., E.C., and E.B. interpreted and discussed the experimental results. M. S.-P. did the TEM measurements as well as the interpretation of the data. E.B. and T.M. supervised the work and organized the funding. All authors discussed the work and modified the manuscript.

The authors declare that they have no competing interests.

APPENDIX A: DFT RESULTS

1. Different stoichiometries

To study the impact of varying Al concentrations in $Fe_{2-2x}V_{1-x}Al_{1+3x}$, different stoichiometries were analyzed using DFT calculations. The electronic band structures of all calculated compositions ranging from $x = 0$ to $x = 0.22$ are plotted in Fig. 6. The supercells were created on the basis of the most stable antisite configuration (AC) of $Fe_{1.78}V_{0.89}Al_{1.33}$, randomly adding or removing the respective amount of substitutional Al antisites. For the different Al concentrations, again different antisite configurations were tested and the stability of the DOSs against changes in the ACs was analyzed. As an example, the stability of the electronic DOS for different antisite configurations of $Fe_{1.7}V_{0.85}Al_{1.45}$ is demonstrated for the respective band structures of three different ACs in Fig. S1C of the Supplemental Material [23].

APPENDIX B: STRUCTURAL CHARACTERIZATION

1. X-ray diffraction

The lattice parameters depicted in Fig. 4(a) were extracted from X-ray diffraction using Rietveld refinement as implemented in the crystallographic software PowderCell. The fit of the model on the raw data of $Fe_{1.78}V_{0.89}Al_{1.33}$ is shown as an example in Fig. 7. Although the absolute peak heights and widths of full-Heusler materials can be affected by grinding during preparation for powder diffraction [131], the refinement shows excellent agreement.

2. Transmission electron microscopy

To ensure full homogeneity also at medium scales, the $Fe_{1.78}V_{0.89}Al_{1.33}$ sample was also analyzed using TEM with lower magnifications. At the lower microscale, precipitates of V_4Al_4C can be detected (see Fig. 8). Their volume fraction is far less than 1% and thus their influence on the material properties is negligible. Furthermore, the energy loss by channeled electrons (ELCE) method was employed to probe the distribution of the Al antisites on the Fe and V sites, respectively. Using electron energy-loss spectroscopy (EELS), the Bloch-wave symmetry can be exploited to obtain site-selective information on the constituent elements. The different EELS spectra reveal an apparent trend of Al substitution at the Fe and V sites (see Fig. 9).

APPENDIX C: ADDITIONAL MEASUREMENT DATA

1. Magnetization measurements

To measure the magnetization, cubic pieces of about 50 mg were cut out of the samples and mounted on a brass sample holder to be used for the vibrating-sample magnetometer (VSM). The commercially available VSM insert for the physical-properties measurement system (PPMS) from Quantum Design was used to conduct the measurement. We used a vibration frequency of 20 Hz to achieve a good signal-to-noise ratio. First, a field sweep at room temperature from −9 to 9 T was measured. The temperature-dependent magnetization was then measured from 300 to 2 K, with a cooling rate of 10 K/min, applying a field of 0.1 T. Furthermore, magnetic field sweeps were done from −9 to 9 T at 20 and 2 K with a sweeping rate of 0.01 T/s, interrupting the cool-down. Another temperature-dependent sweep was done while warming up from 1.9 to 300 K, with a rate of 3 K/min and a magnetic field of 1 T.

As shown in Fig. 1, the synthesized $Fe_{2-2x}V_{1-x}Al_{1+3x}$ samples in this work do not follow the S-P prediction of their electronic structure regarding the band gap as well as the magnetic properties. While the S-P rule predicts a magnetic moment of

$$M = N_V - 24\ \mu_B/\text{f.u.}, \tag{C1}$$

the semiconducting band structure with fully filled Fe valence bands and unfilled V-dominated conduction bands precludes spin polarization. Indeed, spin-polarized calculations were performed and showed no discrepancy between majority and minority spins in the DOS. The magnetic properties of pristine Fe_2VAl found in the literature vary strongly because of different synthesis methods and annealing conditions. It is generally established as a nonmagnetic semimetal, containing magnetic antisite defects. For an Fe_V antisite pair, it has been shown experimentally as well as theoretically that it exhibits a magnetic moment of 3.7 μB. These impurities can form magnetic clusters and lead to superparamagnetic behavior in the experimental compound [132].

In this work, Fe and V atoms are actively replaced by Al, reducing the valence electron concentration from 24 e^- per f.u. down to values as low as 21.6 e^- per f.u. Following the S-P rule [Eq. (C1)], this should lead to strong magnetic moments of 1.3 and 2.4 μ_B per f.u. for $x = 0.11$ and $x = 0.2$, respectively.

However, the temperature-dependent magnetization shown in Fig. 10(a), measured at $H = 1$ T, reveals very low absolute values and apparent paramagnetic behavior, with the magnetization M rising in a $1/T$ manner toward low temperatures. As the absolute values of the magnetization are very low, with around 0.006 μ_B per f.u. at 1 T at 1.9 K, it is certain that the bulk of the sample is not ferromagnetic, demonstrating the violation of the S-P rule in these compounds.

Moreover, the absolute magnetization drops notably with increasing Al substitution, compared to the pristine material, as illustrated in the inset of Fig. 10(a). This behavior indicates a reduction of magnetic Fe antisite

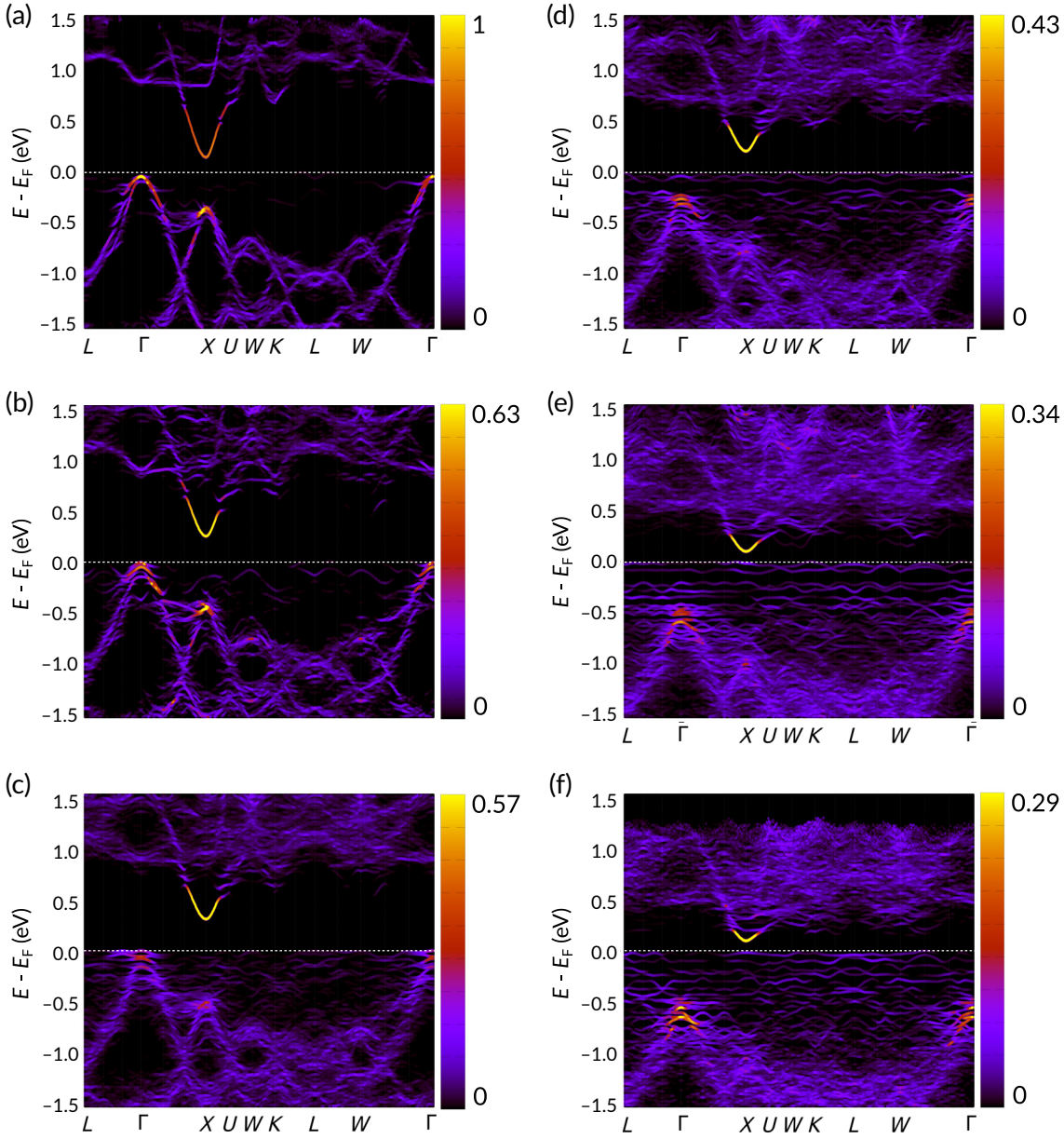

FIG. 6. The band structures of $Fe_{2-2x}V_{1-x}Al_{1+3x}$ for different Al concentrations. (a)–(f) The spectral functions $A(k, E_F)$ extracted from the unfolded band-structure calculations of $Fe_{2-2x}V_{1-x}Al_{1+3x}$ for $x = 0.04, 0.07, 0.11, 0.15, 0.19$ and 0.22. For $x \leq 0.11$, a clear transition from a pseudogap system to a semiconductor can be observed, while for higher x, the impurity bands are shifted into the gap, effectively reducing it. In general, the edge of the V-dominated band at the X point of the Brillouin zone is shifted toward higher energies and broadens with increasing Al substitution. For very high antisite concentrations x, the band structure becomes decoherent, as the periodicity of the lattice is heavily disturbed.

defects by increasing amounts of excess Al atoms, which can be made plausible by the excess of Al antisites suppressing other defects.

The absence of ferromagnetism in the off-stoichiometric $Fe_{2-2x}V_{1-x}Al_{1+3x}$ compounds is highlighted through a comparison with $Mn_{2-y}Co_yAl$ full-Heusler compounds, which adhere to the S-P rule. As shown in Fig. 10(b), this comparison underscores the substantial difference in magnetization between the two material systems.

2. Analysis of the Seebeck coefficient

The temperature-dependent Seebeck-coefficient data were fitted using a three parabolic band model as described in Sec. II. The raw experimental data are shown in Fig. 11 as the colored points. The respective curves resulting from the fits are plotted as solid lines in the same color. The extracted fit parameters, which lead to the plotted theoretical curves, are presented in Table S2 of the Supplemental Material [23]. For completeness, the simple analysis with

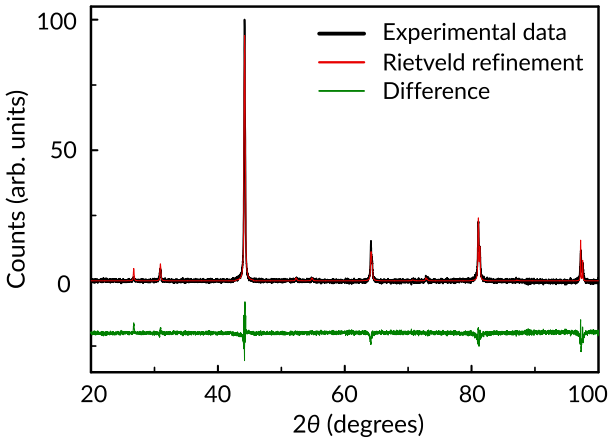

FIG. 7. The Rietveld refinement of the XRD pattern. An example of Rietveld refinement shown for $Fe_{1.78}V_{0.89}Al_{1.33}$, with normalized counts over the diffraction angle 2θ. The experimental XRD pattern is depicted as the black line, while the fitted crystal structure is depicted by the solid red line. The difference between experiment and theory is plotted as the green solid line at the bottom. From the refinement, the lattice parameter of the sample has been determined to $a = 5.81$ Å.

the Goldsmid-Sharp (GS) formula for estimating the band gap in semiconductors was conducted. For a measurement curve with the maximum Seebeck $S_{\max}$ and the respective temperature at the maximum $T_{\max}$, the band gap E_g of the sample can be estimated as [128]

$$E_g \approx 2e|S_{\max}|T_{\max}. \tag{C2}$$

Applying this formula yields a similar behavior for the composition-dependent evolution of the band gap for the

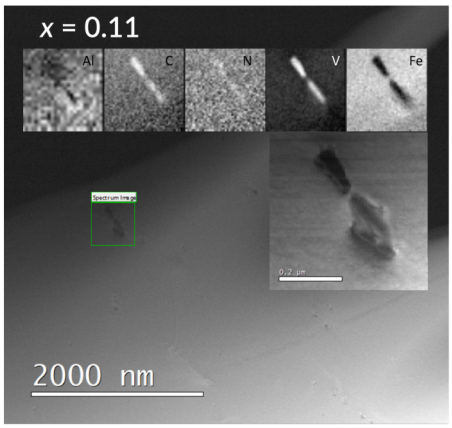

FIG. 8. A TEM image of $Fe_{1.78}V_{0.89}Al_{1.33}$. Small precipitates of V_4Al_4C are observable at medium magnifications. They are likely caused by small amounts of carbon contained in the raw elements. Their volume fraction has been estimated to be smaller than 1%.

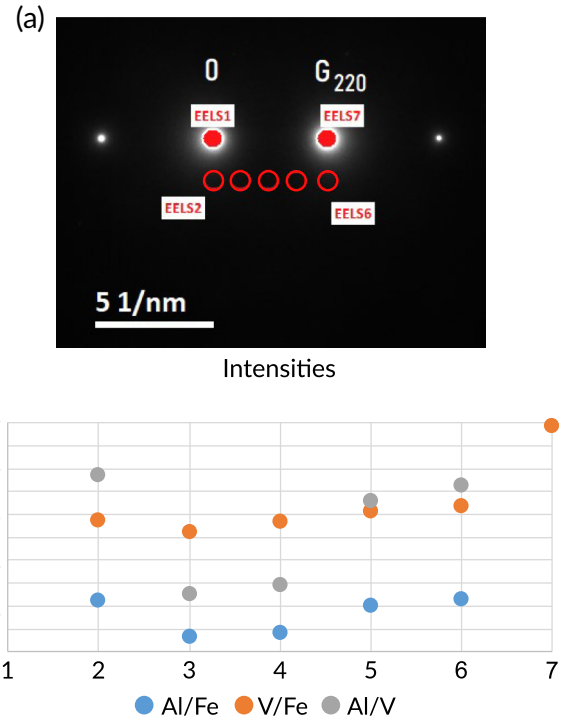

FIG. 9. The EELS analysis of the site occupancies of the Fe,V, and Al atoms. (a) The different momenta of the channeled electron beam used to analyze the site occupancy in the sample. We measured between the 000 symmetry reflection and the 220 symmetry of the crystal. (b) An analysis of the energy loss by channeled electrons in $Fe_{1.78}V_{0.89}Al_{1.33}$. A similar trend of V-Fe and Al-Fe site occupation for the angular-dependent electron energy-loss spectra is observable, indicating an equal distribution of Al antisites on the respective lattice sites.

$Fe_{2-2x}V_{1-x}Al_{1+3x}$ sample series, with a maximum evolving around $x = 0.11$ [see Fig. 12(d)]. However, the absolute values of E_g are significantly underestimated by a factor of around 2 for the system presented here. It is well known that the GS formula can lead to erroneous results for small-gap systems [133]. This is mainly due to the assumption of equal effective masses of the relevant bands $m_2/m_1 = 1$, which is not the case in this study. Especially for majority carriers with higher effective mass, this can lead to an underestimation of the band gap E_g. Therefore, this formula gives an easy but only crude estimation for the band gap. For the $Fe_{2-2x}V_{1-x}Al_{1+3x}$ compounds, there is a large discrepancy between the band masses of the valence and conduction bands. Hence, the parabolic band model is a better tool for estimating the electronic structure of this system, as also discussed in the main text.

3. Analysis of electrical resistivity

To corroborate the experimental results in the main text, the electrical resistivities of selected samples of $Fe_{2-2x}V_{1-x}Al_{1+3x}$ with x ranging from 0 tp 0.2 were

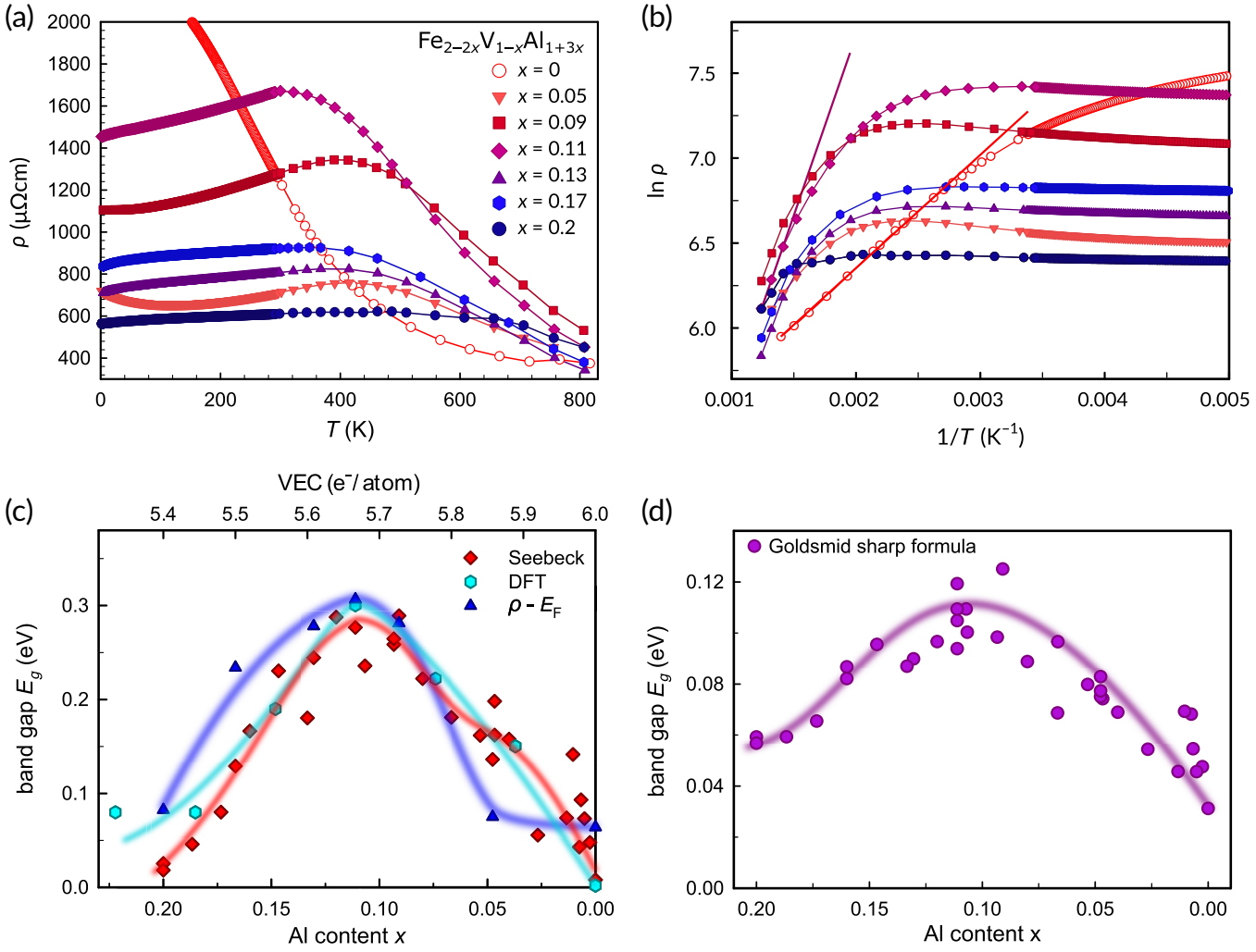

FIG. 12. An analysis of the electrical resistivity of the $Fe_{2-2x}V_{1-x}Al_{1+3x}$ compounds. (a) The temperature-dependent electrical resistivity $\rho(T)$ for different x in the range $0 \leq x \leq 0.2$. At low temperatures, the resistivity behavior is reminiscent of bad metals, while at high temperatures, the resistivity drops due to the contribution of the conduction band. (b) The Arrhenius plot, showcasing activated behavior across an energy gap at high temperatures, by plotting $\ln\rho(T)$ versus $1/T$. For $x = 0$ and $x = 0.11$; as an example, the fit is drawn as a straight solid line. (c) A comparison of the extracted band gaps from the DFT calculations, the analysis of $S(T)$, and the analysis of $\rho(T)$. The band gap obtained from the Arrhenius relation has been adjusted by substracting the energy difference of the Fermi level E_F to the valence-band edge from the extracted transport gap, as these samples are slightly doped. (d) The extracted band gap from the temperature-dependent Seebeck-coefficient data using the simple Goldsmid-Sharp formula [128].

analyzed regarding their temperature-dependent behavior at high temperatures, where thermal activation across the band gap leads to a semiconductinglike behavior ($d\rho/dT < 0$). The measurement data, obtained from Ref. [105], are depicted in Fig. 12(a). To keep the plot manageable, only specific compositions along the transition from $x = 0 - 0.2$ have been plotted. Apart from Fe_2VAl ($x = 0$), all samples show metallic resistivity behavior at low temperatures, as the Fermi level is intrinsically doped inside the valence band due to Fe_V exchange antisite defects. As discussed in Ref. [104], the residual resistivity ratio (RRR) of the *metallic* behavior is very low and decreases with increasing x. At high temperatures, the conduction band becomes relevant for electronic transport, leading to a significant decrease of the resistivity, which is also reflected in the Seebeck data at similar temperatures (see Fig. 11). This activated behavior can be fitted with the Arrhenius relation, to obtain an estimate for the effective transport gap from the electrical-resistivity data:

$$\rho(T) \approx Ae^{E_g/2k_BT}, \tag{C3}$$

where k_B is the Boltzmann constant and E_g and A are the fitting parameters. To visualize this relation, in Fig. 12(b) we show $ln(\rho(T))$ vs $1/T$. Two fits for $x = 0$ and $x = 0.11$, which exhibit significant transport gaps, are depicted as

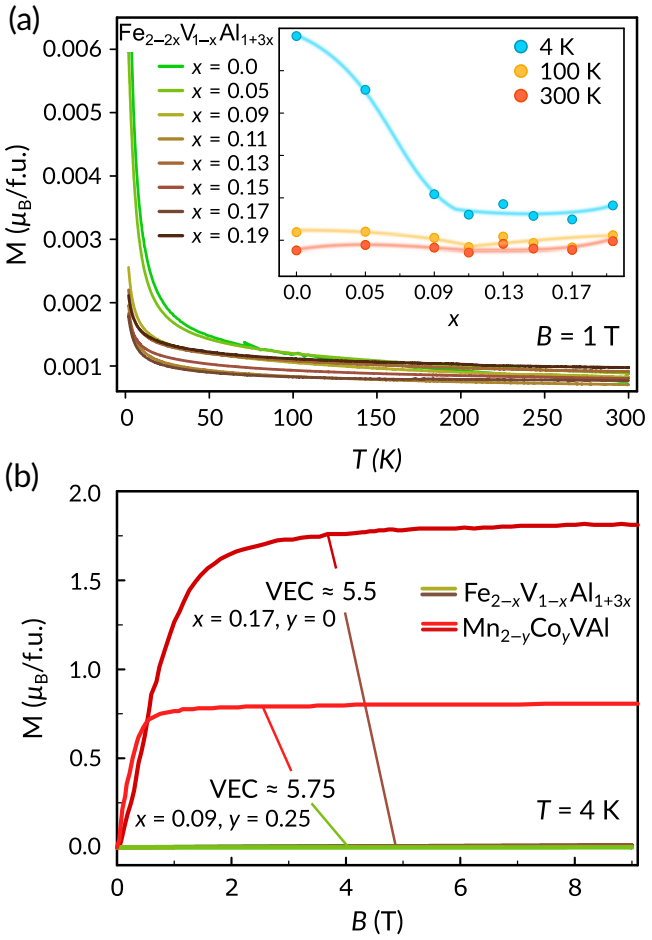

FIG. 10. The magnetic properties of the $Fe_{2-2x}V_{1-x}Al_{1+3x}$ samples. (a) The temperature-dependent magnetization for different Al concentrations x at a field of $B = 1$ T. The inset highlights the decrease of magnetization with rising Al at low temperatures. (b) A comparison of the magnetization of the $Fe_{2-2x}V_{1-x}Al_{1+3x}$ compounds with the full-Heusler system $Mn_{2-y}Co_yVAl$ [38], obeying the S-P rule. A clear distinction can be made, as the magnetization values of the off-stoichiometric Heuslers presented here are magnitudes lower, ruling out ferromagnetic ordering in these samples.

representative examples. To compare the transport gaps obtained from the Arrhenius relation with the band gap, we have subtracted it with the position of the Fermi level with respect to the valence-band edge, obtained from the Seebeck fit. While it is a rough approximation, as only few measurement points have been taken at the relevant temperatures, the results shown in Fig. 12(c) are quite convincing. Again, the absolute values for the band gap E_g obtained from fitting $\rho(T)$ are in agreement with the values obtained from fitting the temperature-dependent Seebeck, as well as the values obtained from our DFT calculations. While the composition dependence shows some deviations, a clear maximum of E_g evolves around the composition of $x = 0.11$. This is further confirmation of the band gap opening in these compounds and the interesting electronic structure of the $Fe_{2-2x}V_{1-x}Al_{1+3x}$ compounds.

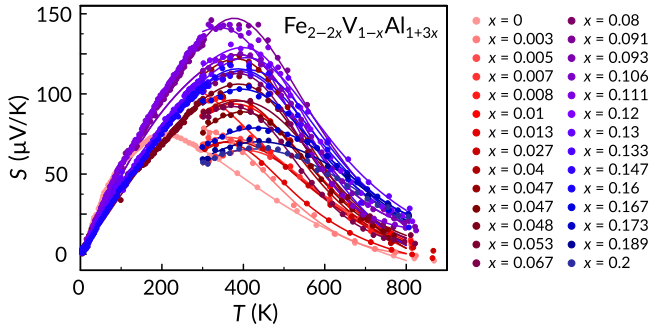

FIG. 11. The Seebeck coefficient of the measured $Fe_{2-2x}V_{1-x}Al_{1+3x}$ samples with the respective fits. The temperature-dependent thermopower data of all measured samples of $Fe_{2-2x}V_{1-x}Al_{1+3x}$. The points depict the measured values, while the solid lines represent the curves of the fitting procedure to approximate the effective band structure. For every $S(T)$ curve, the fit is very close to the experiment. The resulting fitting parameters can be found in Table S2 of the Supplemental Material [23].

[1] T. Graf, C. Felser, and S. S. Parkin, Simple rules for the understanding of Heusler compounds, Prog. Solid State Chem. **39**, 1 (2011).

[2] I. Galanakis, P. Dederichs, and N. Papanikolaou, Slater-Pauling behavior and origin of the half-metallicity of the full-Heusler alloys, Phys. Rev. B **66**, 174429 (2002).

[3] B. Yan and C. Felser, Topological materials: Weyl semimetals, Annu. Rev. Condens. Matter Phys. **8**, 337 (2017).

[4] T. Klimczuk, C. Wang, K. Gofryk, F. Ronning, J. Winterlik, G. H. Fecher, J.-C. Griveau, E. Colineau, C. Felser, J. D. Thompson, *et al.*, Superconductivity in the Heusler family of intermetallics, Phys. Rev. B **85**, 174505 (2012).

[5] K. Manna, Y. Sun, L. Muechler, J. Kübler, and C. Felser, Heusler, Weyl and Berry, Nat. Rev. Mater. **3**, 244 (2018).

[6] F. Casper, T. Graf, S. Chadov, B. Balke, and C. Felser, Half-Heusler compounds: Novel materials for energy and spintronic applications, Semicond. Sci. Technol. **27**, 063001 (2012).

[7] C. Felser, L. Wollmann, S. Chadov, G. H. Fecher, and S. S. Parkin, Basics and prospective of magnetic Heusler compounds, APL Mater. **3**, 041518 (2015).

[8] T. Zhu, C. Fu, H. Xie, Y. Liu, and X. Zhao, High efficiency half-Heusler thermoelectric materials for energy harvesting, Adv. Energy Mater. **5**, 1500588 (2015).

[9] F. Garmroudi, M. Parzer, A. Riss, S. Beyer, S. Khmelevskyi, T. Mori, M. Reticcioli, and E. Bauer, Large thermoelectric power factors by opening the band gap in semimetallic Heusler alloys, Mater. Today Phys. **27**, 100742 (2022).

[10] F. Garmroudi, A. Riss, M. Parzer, N. Reumann, H. Müller, E. Bauer, S. Khmelevskyi, R. Podloucky, T. Mori, K. Tobita, *et al.*, Boosting the thermoelectric performance of Fe_2VAl-type Heusler compounds by band engineering, Phys. Rev. B **103**, 085202 (2021).

[11] K. Fukuta, K. Tsuchiya, H. Miyazaki, and Y. Nishino, Improving thermoelectric performance of Fe_2VAl-based Heusler compounds via high-pressure torsion, Appl. Phys. A **128**, 1 (2022).

[12] F. Garmroudi, M. Parzer, A. Riss, A. V. Ruban, S. Khmelevskyi, M. Reticcioli, M. Knopf, H. Michor, A. Pustogow, T. Mori, *et al.*, Anderson transition in stoichiometric Fe_2VAl: High thermoelectric performance from impurity bands, Nat. Commun. **13**, 1 (2022).

[13] T. Fujimoto, M. Mikami, H. Miyazaki, and Y. Nishino, Enhanced thermoelectric performance of Ru_2TiSi Heusler compounds with Ta substitution, J. Alloys. Compd. **969**, 172345 (2023).

[14] E. Alleno, A. Diack-Rasselio, M. T. Noutack, and P. Jund, Optimization of the thermoelectric properties in self-substituted Fe_2VAl, Phys. Rev. Mater. **7**, 075403 (2023).

[15] D. Bourgault, H. Hajoum, R. Haettel, and E. Alleno, Unlocking microwatt power: Enhanced performance of Fe-V-Al thin films in thermoelectric microgenerators, J. Mater. Chem. A **11**, 19556 (2023).

[16] Y. Takagiwa and Y. Iwasaki, Effect of off-stoichiometry and point defects on thermoelectric properties of a W-substituted Fe_2VAl Heusler compound, ACS Appl. Energy Mater. **6**, 8256 (2023).

[17] R. Jha, N. Tsujii, F. Garmroudi, S. Khmelevskyi, E. Bauer, and T. Mori, Unexpected p-type thermoelectric transport arising from magnetic Mn substitution in $Fe_2V_{1-x}Mn_xAl$ Heusler compounds, J. Mater. Chem. C **12**, 8861 (2024).

[18] See the Supplemental Material at http://link.aps.org/supplemental/10.1103/PRXEnergy.3.033006. The Supplemental Material file is a spreadsheet, containing all the literature data necessary to reconstruct Fig. 1(a), 1(b). It is taken from extensive literature research. It is sorted by the number of valence electrons per atom, of the respective compounds.

[19] J. C. Slater, Electronic structure of alloys, J. Appl. Phys. **8**, 385 (1937).

[20] L. Pauling, The nature of the interatomic forces in metals, Phys. Rev. **54**, 899 (1938).

[21] H. C. Kandpal, C. Felser, and R. Seshadri, Covalent bonding and the nature of band gaps in some half-Heusler compounds, J. Phys. D: Appl. Phys. **39**, 776 (2006).

[22] K. Ciesielski, K. Synoradzki, I. Veremchuk, P. Skokowski, D. Szymański, Y. Grin, and D. Kaczorowski, Thermoelectric performance of the half-Heusler phases RNiSb (R = Sc, Dy, Er, Tm, Lu): High mobility ratio between majority and minority charge carriers, Phys. Rev. Appl. **14**, 054046 (2020).

[23] See the Supplemental Material at http://link.aps.org/supplemental/10.1103/PRXEnergy.3.033006 for additional results from DFT calculations and a table of the three parabolic band model fitting results (including Refs. [83,134–137]).

[24] B. Abu Alhaj and B. Hamad. J. Appl. Phys. **112**, 123904 (2012).

[25] K. Nagai, H. Fujiwara, H. Aratani, S. Fujioka, H. Yomosa, Y. Nakatani, T. Kiss, A. Sekiyama, F. Kuroda, H. Fujii, T. Oguchi, A. Tanaka, J. Miyawaki, Y. Harada, Y. Takeda, Y. Saitoh, S. Suga, and R. Y. Umetsu. Phys. Rev. B **97**, 035143 (2018).

[26] H. C. Kandpal, G. H. Fecher, and C. Felser. J. Phys. D: Appl. Phys. **40**, 1507 (2007).

[27] S. Berri, M. Ibrir, D. Maouche, and M. Attallah. Comput. Condens. Matter **1**, 26 (2014).

[28] X.-H. Kang and J.-M. Zhang. J. Phys. Chem. Solids **105**, 9 (2017).

[29] R. Dhakal, S. Nepal, I. Galanakis, R. P. Adhikari, and G. C. Kaphle. J. Alloys Compd. **882**, 160500 (2021).

[30] S. Skaftouros, K. Özdoğan, E. Şaşıoğlu, and I. Galanakis. Phys. Rev. B **87**, 024420 (2013).

[31] S. Skaftouros, K. Özdoğan, E. Şaşıoğlu, and I. Galanakis. Appl. Phys. Lett. **102**, 022402 (2013).

[32] M. Benkabou, H. Rached, A. Abdellaoui, D. Rached, R. Khenata, M. Elahmar, B. Abidri, N. Benkhettou, and S. Bin-Omran. J. Alloys Compd. **647**, 276 (2015).

[33] S. M. Zareii, H. Arabi, and R. Sarhaddi. Phys. B **407**, 3339 (2012).

[34] G. H. Fecher and C. Felser. J. Phys. D: Appl. Phys. **40**, 1582 (2007).

[35] K. Özdoğan, E. Şaşıoğlu, and I. Galanakis. J. Phys. D: Appl. Phys. **42**, 085003 (2009).

[36] I. Galanakis and P. Mavropoulos. J. Phys.: Condens. Matter **19**, 315213 (2007).

[37] X. Feng, L. Feng, C. Guo, and W. Zhang. Comput. Mater. Sci. **127**, 15 (2017).

[38] Q. F. Li, H. F. Zhao, X. Zhong, and J. L. Su, Co doping effects on structural, electronic and magnetic properties in Mn_2VGa, J. Magn. Magn. Mater. **324**, 1463 (2012).

[39] R. Gavrea, A. Bolinger, V. Pop, O. Isnard, M. Coldea, and D. Benea. Phys. Status Solidi B **254**, 1700160 (2017).

[40] V. Jain, V. Jain, V. Sudheesh, N. Lakshmi, and K. Venugopalan, in *AIP Conference Proceedings* (American Institute of Physics), Vol. 1591, pp. 1544–1545 (2014).

[41] B. Deka, A. Srinivasan, R. Singh, B. C. S. Varaprasad, Y. Takahashi, and K. Hono. J. Alloys Compd. **662**, 510 (2016).

[42] I. Galanakis, P. Mavropoulos, and P. H. Dederichs. J. Phys. D: Appl. Phys. **39**, 765 (2006).

[43] K. Özdoğan, E. Şaşıoğlu, B. Aktaş, and I. Galanakis. Phys. Rev. B **74**, 172412 (2006).

[44] J. Kübler, G. Fecher, and C. Felser. Phys. Rev. B **76**, 024414 (2007).

[45] D. I. Bilc, G. Hautier, D. Waroquiers, G.-M. Rignanese, and P. Ghosez. Phys. Rev. Lett. **114**, 136601 (2015).

[46] H. Zhu, J. Mao, Y. Li, J. Sun, Y. Wang, Q. Zhu, G. Li, Q. Song, J. Zhou, Y. Fu and R. He. Nat. Commun. **10**, 270 (2019).

[47] T. Fang, S. Zheng, H. Chen, H. Cheng, L. Wang, and P. Zhang. RSC Adv. **6**, 10507 (2016).

[48] F. Shi, M. Si, J. Xie, K. Mi, C. Xiao, and Q. Luo. J. Appl. Phys. **122**, 215701 (2017).

[49] K. K. Johari, R. Bhardwaj, N. S. Chauhan, B. Gahtori, S. Bathula, S. Auluck, and S. Dhakate. ACS Appl. Energy Mater. **3**, 1349 (2019).

[50] M.-S. Lee, F. P. Poudeu, and S. Mahanti. Phys. Rev. B **83**, 085204 (2011).
[51] L. Wang, Z. Dong, S. Tan, J. Zhang, W. Zhang, and J. Luo. Adv. Funct. Mater. **32**, 2200438 (2022).
[52] S. Anand and G. J. Snyder. ACS Appl. Electron. Mater. **4**, 3392 (2022).
[53] B. Balke, S. Ouardi, T. Graf, J. Barth, C. G. Blum, G. H. Fecher, A. Shkabko, A. Weidenkaff, and C. Felser. Solid State Commun. **150**, 529 (2010).
[54] A. Yamasaki, S. Imada, R. Arai, H. Utsunomiya, S. Suga, T. Muro, Y. Saitoh, T. Kanomata, and S. Ishida. Phys. Rev. B **65**, 104410 (2002).
[55] W. G. Zeier, S. Anand, L. Huang, R. He, H. Zhang, Z. Ren, C. Wolverton, and G. J. Snyder, Using the 18-electron rule to understand the nominal 19-electron half-Heusler NbCoSb with Nb vacancies, Chem. Mater. **29**, 1210 (2017).
[56] J. Miranda and T. Gruhn. J. Electron. Mater. **51**, 2043 (2022).
[57] S. Wurmehl, H. C. Kandpal, G. H. Fecher, and C. Felser. J. Phys.: Condens. Matter **18**, 6171 (2006).
[58] T. Graf, J. Barth, C. G. Blum, B. Balke, C. Felser, P. Klaer, and H.-J. Elmers. Phys. Rev. B **82**, 104420 (2010).
[59] T. Block, C. Felser, G. Jakob, J. Ensling, B. Mühling, P. Gütlich, and R. Cava. J. Solid State Chem. **176**, 646 (2003).
[60] P. Webster. J. Phys. Chem. Solids **32**, 1221 (1971).
[61] H. Ido and S. Yasuda. J. Phys. Colloques **49**, C8 (1988).
[62] K. Yoshimura, A. Miyazaki, R. Vijayaraghavan, and Y. Nakamura. J. Magn. Magn. Mater. **53**, 189 (1985).
[63] K. Özdoğan, E. Şaşıoğlu, and I. Galanakis. J. Appl. Phys. **113** (2013).
[64] S. Chadov, G. H. Fecher, C. Felser, J. Minár, J. Braun, and H. Ebert. J. Phys. D: Appl. Phys. **42**, 084002 (2009).
[65] B. G. Yalcin. J. Magn. Magn. Mater. **408**, 137 (2016).
[66] S. A. Khandy. Mater. Res. Express **5**, 056516 (2018).
[67] S. A. Khandy, I. Islam, D. C. Gupta, and A. Laref. Int. J. Energy Res. **42**, 4221 (2018).
[68] S. A. Khandy and D. C. Gupta. Semicond. Sci. Technol. **32**, 125019 (2017).
[69] S. A. Khandy and J.-D. Chai. J. Magn. Magn. Mater. **487**, 165289 (2019).
[70] S. Ishida, S. Akazawa, Y. Kubo, and J. Ishida. J. Phys. F: Metal Phys. **12**, 1111 (1982).
[71] B. Gurunani and D. C. Gupta. Sci. Rep. **13**, 22834 (2023).
[72] P. Midhunlal, C. Venkatesh, J. A. Chelvane, P. Babu, and N. H. Kumar. J. Phys.: Condens. Matter **34**, 125801 (2022).
[73] D. R. Jaishi, S. Bati, N. Sharma, B. Karki, B. P. Belbase, and M. P. Ghimire. Phys. Chem. Chem. Phys. **24**, 19844 (2022).
[74] P. V. Lukashev, J. Wysong, S. McFadden, G. Baker, B. Schmidt, P. M. Shand, and P. Kharel. J. Phys.: Condens. Matter **36**, 085801 (2023).
[75] S. A. Khandy and J.-D. Chai. J. Appl. Phys. **127** (2020).
[76] S. A. Khandy. Sci. Rep. **11**, 20756 (2021).
[77] H. Alqurashi and B. Hamad. Appl. Phys. A **127**, 799 (2021).
[78] M. Benidris, Z. Aziz, M. A. Bennani, M. Matougui, S. Terkhi, M. Houari, B. Bouadjemi, and S. A. Khandy. Solid State Commun. **339**, 114466 (2021).
[79] L. Boumia, F. Dahmane, B. Doumi, D. Rai, S. A. Khandy, H. Khachai, H. Meradji, A. H. Reshak, and R. Khenata. Chin. J. Phys. **59**, 281 (2019).
[80] D. C. Gupta and I. H. Bhat. J. Magn. Magn. Mater. **374**, 209 (2015).
[81] H. Luo, Q. Li, K. Sun, S. Liu, and Z. Liang. J. Magn. Magn. Mater. **496**, 165908 (2020).
[82] R. Bentata, S. Bentata, B. Bouadjemi, T. Lantri, and D. Chenine. Chin. J. Phys. **59**, 28 (2019).
[83] S. Mondal, C. Mazumdar, R. Ranganathan, E. Alleno, P. Sreeparvathy, V. Kanchana, and G. Vaitheeswaran, Ferromagnetically correlated clusters in semimetallic Ru_2NbAl Heusler alloy and its thermoelectric properties, Phys. Rev. B **98**, 205130 (2018).
[84] G. Liu, X. Dai, H. Liu, J. Chen, Y. Li, G. Xiao, and G. Wu. Phys. Rev. B **77**, 014424 (2008).
[85] Q. Li, C. Yang, and J. Su. Phys. B **406**, 3726 (2011).
[86] J. Ma, V. I. Hegde, K. Munira, Y. Xie, S. Keshavarz, D. T. Mildebrath, C. Wolverton, A. W. Ghosh, and W. Butler. Phys. Rev. B **95**, 024411 (2017).
[87] B. Shi, J. Li, C. Zhang, W. Zhai, S. Jiang, W. Wang, D. Chen, Y. Yan, G. Zhang, and P.-F. Liu. Phys. Chem. Chem. Phys. **22**, 23185 (2020).
[88] D. W. Hook, S. J. Porter, and C. Herzog, Dimensions: Building context for search and evaluation, Front. Res. Metr. Anal. **3**, 23 (2018).
[89] S. Anand, K. Xia, V. I. Hegde, U. Aydemir, V. Kocevski, T. Zhu, C. Wolverton, and G. J. Snyder, A valence balanced rule for discovery of 18-electron half-Heuslers with defects, Energy Environ. Sci. **11**, 1480 (2018).
[90] C.-S. Lue, R.-F. Liu, M. Song, K. Wu, and Y. Kuo, Chemical pressure effect on the transport and electronic band structure of $Fe_2V_{1-x}Nb_xAl$, Phys. Rev. B **78**, 165117 (2008).
[91] M. Meinert, M. P. Geisler, J. Schmalhorst, U. Heinzmann, E. Arenholz, W. Hetaba, M. Stöger-Pollach, A. Hütten, and G. Reiss, Experimental realization of a semiconducting full-Heusler compound: Fe_2TiSi, Phys. Rev. B **90**, 085127 (2014).
[92] S. Anand, M. Wood, Y. Xia, C. Wolverton, and G. J. Snyder, Double half-Heuslers, Joule **3**, 1226 (2019).
[93] L. Wang, Z. Dong, S. Tan, J. Zhang, W. Zhang, and J. Luo, Discovery of a Slater Pauling semiconductor $ZrRu_{1.5}Sb$ with promising thermoelectric properties, Adv. Funct. Mater. **32**, 2200438 (2022).
[94] L. Huang, R. He, S. Chen, H. Zhang, K. Dahal, H. Zhou, H. Wang, Q. Zhang, and Z. Ren, A new *n*-type half-Heusler thermoelectric material NbCoSb, Mater. Res. Bull. **70**, 773 (2015).
[95] H. Zhang, Y. Wang, L. Huang, S. Chen, H. Dahal, D. Wang, and Z. Ren, Synthesis and thermoelectric properties of *n*-type half-Heusler compound VCoSb with valence electron count of 19, J. Alloys. Compd. **654**, 321 (2016).
[96] K. Xia, Y. Liu, S. Anand, G. J. Snyder, J. Xin, J. Yu, X. Zhao, and T. Zhu, Enhanced thermoelectric performance in 18-electron $Nb_{0.8}CoSb$ half-Heusler compound with intrinsic Nb vacancies, Adv. Funct. Mater. **28**, 1705845 (2018).
[97] L. Huang, T. Liu, A. Huang, G. Yuan, J. Wang, J. Liao, X. Lei, Q. Zhang, and Z. Ren, Enhanced thermoelectric performance of nominal 19-electron half-Heusler compound

NbCoSb with intrinsic Nb and Sb vacancies, Mater. Today Phys. **20**, 100450 (2021).
[98] V. Kanchana, G. Vaitheeswaran, Y. Ma, Y. Xie, A. Svane, and O. Eriksson, Density functional study of elastic and vibrational properties of the Heusler-type alloys Fe_2VAl and Fe_2VGa, Phys. Rev. B **80**, 125108 (2009).
[99] P. Hohenberg and W. Kohn, Inhomogeneous electron gas, Phys. Rev. **136**, B864 (1964).
[100] W. Kohn and L. J. Sham, Self-consistent equations including exchange and correlation effects, Phys. Rev. **140**, A1133 (1965).
[101] G. Kresse and J. Hafner, *Ab initio* molecular dynamics for liquid metals, Phys. Rev. B **47**, 558 (1993).
[102] G. Kresse and J. Furthmüller, Efficiency of ab-initio total energy calculations for metals and semiconductors using a plane-wave basis set, Comput. Mater. Sci. **6**, 15 (1996).
[103] G. Kresse and J. Furthmüller, Efficient iterative schemes for *ab initio* total-energy calculations using a plane-wave basis set, Phys. Rev. B **54**, 11169 (1996).
[104] G. Kresse and D. Joubert, From ultrasoft pseudopotentials to the projector augmented-wave method, Phys. Rev. B **59**, 1758 (1999).
[105] M. Parzer, F. Garmroudi, A. Riss, S. Khmelevskyi, T. Mori, and E. Bauer, High solubility of Al and enhanced thermoelectric performance due to resonant states in Fe_2VAl_x, Appl. Phys. Lett. **120**, 071901 (2022).
[106] M. Stöger-Pollach, USTEM facilities, https://www.tuwien.at/en/research/facilities/ustem/facilities, accessed: 2023-04-19.
[107] R. Resel, E. Gratz, A. Burkov, T. Nakama, M. Higa, and K. Yagasaki, Thermopower measurements in magnetic fields up to 17 tesla using the toggled heating method, Rev. Sci. Instrum. **67**, 1970 (1996).
[108] B. Hinterleitner, P. Fuchs, J. Rehak, F. Garmroudi, M. Parzer, M. Waas, R. Svagera, S. Steiner, M. Kishimoto, R. Moser, *et al.*, Stoichiometric and off-stoichiometric full Heusler $Fe_2V_{1-x}W_xAl$ thermoelectric systems, Phys. Rev. B **102**, 075117 (2020).
[109] F. Garmroudi, M. Parzer, A. Riss, N. Reumann, B. Hinterleitner, K. Tobita, Y. Katsura, K. Kimura, T. Mori, and E. Bauer, Solubility limit and annealing effects on the microstructure & thermoelectric properties of $Fe_2V_{1-x}Ta_xAl_{1-y}Si_y$ Heusler compounds, Acta. Mater. **212**, 116867 (2021).
[110] A. F. May and G. J. Snyder, in *Materials, Preparation, and Characterization in Thermoelectrics*, edited by D. M. Rowe (CRC Press, Boca Raton, FL, 2012), Chap. 11.
[111] S. Bandaru and P. Jund, Electronic structure of the Heusler compound Fe_2VAl and its point defects by *ab initio* calculations, Phys. Status Solidi (B) **254**, 1600441 (2017).
[112] S. Bandaru, A. Katre, J. Carrete, N. Mingo, and P. Jund, Influence of antisite defects on the thermoelectric properties of Fe_2VAl, Nanoscale Microscale Thermophys. Eng. **21**, 237 (2017).
[113] D. I. Bilc and P. Ghosez, Electronic and thermoelectric properties of Fe_2VAl: The role of defects and disorder, Phys. Rev. B **83**, 205204 (2011).
[114] C. Venkatesh, V. Srinivas, V. Rao, S. Srivastava, and P. S. Babu, Effect of site disorder on the electronic properties of Fe_2VAl Heusler alloy, J. Alloys. Compd. **577**, 417 (2013).
[115] M. Haahr, True random number service, Random.org (2023).
[116] S. Anand, R. Gurunathan, T. Soldi, L. Borgsmiller, R. Orenstein, and G. J. Snyder, Thermoelectric transport of semiconductor full-Heusler VFe_2Al, J. Mater. Chem. C **8**, 10174 (2020).
[117] D. Dirnberger, G. Kresse, C. Franchini, and M. Reticcioli, BANDS4VASP postprocessing package, https://github.com/QuantumMaterialsModelling/bands4vasp (2021).
[118] D. Dirnberger, G. Kresse, C. Franchini, and M. Reticcioli, Electronic state unfolding for plane waves: Energy bands, fermi surfaces, and spectral functions, J. Phys. Chem. C **125**, 12921 (2021).
[119] M. Weinert and R. Watson, Hybridization-induced band gaps in transition-metal aluminides, Phys. Rev. B **58**, 9732 (1998).
[120] K. Sun, Z. Gu, H. Katsura, and S. D. Sarma, Nearly flatbands with nontrivial topology, Phys. Rev. Lett. **106**, 236803 (2011).
[121] L. Balents, C. R. Dean, D. K. Efetov, and A. F. Young, Superconductivity and strong correlations in Moiré flat bands, Nat. Phys. **16**, 725 (2020).
[122] L.-S. Hsu, Y.-K. Wang, G. Guo, and C. S. Lue, Experimental and theoretical study of the electronic structure of Fe_3Al, Fe_2VAl, and Fe_2VGa, Phys. Rev. B **66**, 205203 (2002).
[123] B. Hinterleitner, F. Garmroudi, N. Reumann, T. Mori, E. Bauer, and R. Podloucky, The electronic pseudo band gap states and electronic transport of the full-Heusler compound Fe_2VAl, J. Mater. Chem. C **9**, 2073 (2021).
[124] H. Li, K. Hayashi, and Y. Miyazaki, Design and fabrication of full-Heusler compound with positive Seebeck coefficient as a potential thermoelectric material, Scr. Mater. **150**, 130 (2018).
[125] H. Li, Ph.D. thesis, Tohoku University, Sendai, Japan, 2022.
[126] E. Shreder, A. Filanovich, E. Chernov, A. Lukoyanov, V. Marchenkov, and L. Stashkova, The electronic structure, thermoelectric, and optical properties of Heusler alloys Mn_2MeAl (Me = Ti, V, Cr), Phys. Met. Metallogr. **124**, 684 (2023).
[127] H. Li, K. Hayashi, Z. Huang, H. Takeuchi, G. Kanno, J.-F. Li, and Y. Miyazaki, Enhancement of the thermoelectric performance of half-metallic full-Heusler Mn_2VAl alloys via antisite defect engineering and Si partial substitution, J. Mater. **10**, 511 (2024).
[128] H. Goldsmid and J. Sharp, Estimation of the thermal band gap of a semiconductor from Seebeck measurements, J. Electron. Mater. **28**, 869 (1999).
[129] Y. Nishino, S. Kamizono, H. Miyazaki, and K. Kimura, Effects of off-stoichiometry and Ti doping on thermoelectric performance of Fe_2VAl Heusler compound, AIP Adv. **9**, 125003 (2019).
[130] M. Parzer, Ph.D. thesis, Technische Universität Wien, Vienna, Austria, 2024.
[131] S. Maier, S. Denis, S. Adam, J.-C. Crivello, J.-M. Joubert, and E. Alleno, Order-disorder transitions in the Fe_2VAl Heusler alloy, Acta Mater. **121**, 126 (2016).

[132] C. Lue, J. H. Ross Jr., K. Rathnayaka, D. Naugle, S. Wu, and W. Li, Superparamagnetism and magnetic defects in Fe_2VAl and Fe_2VGa, J. Phys.: Condens. Matter **13**, 1585 (2001).

[133] Z. M. Gibbs, H.-S. Kim, H. Wang, and G. J. Snyder, Band gap estimation from temperature dependent Seebeck measurement—deviations from the $2e|S|_{\max}T_{\max}$ relation, Appl. Phys. Lett. **106**, 022112 (2015).

[134] B. Hamad, Ab initio investigations of the structural, electronic, and thermoelectric properties of Fe_2NbAl-based alloys, J. Mater. Sci. **51**, 10887 (2016).

[135] S. A. Khandy, I. Islam, D. C. Gupta, R. Khenata, and A. Laref, Lattice dynamics, mechanical stability and electronic structure of Fe-based Heusler semiconductors, Sci. Rep. **9**, 1 (2019).

[136] B. Ramachandran, Y. Lin, Y. Kuo, C. Kuo, A. Gippius, and C. Lue, Thermoelectric properties of Heusler-type $Ru_2VAl_{1-x}Ga_x$ alloys, Intermetallics **92**, 36 (2018).

[137] M. Zhang, E. Brück, F. R. de Boer, and G. Wu, Electronic structure, magnetism, and transport properties of the Heusler alloy Fe_2CrAl, J. Magn. Magn. Mater. **283**, 409 (2004).